International Journal of Nanomedicine

Dovepress
Taylor & Francis Group

Open Access Full Text Article

ORIGINAL RESEARCH

Chitosan-Hyaluronic Acid Composite Hydrogel with Slow-Release Hydrogen Sulfide and Cerium Oxide for Multifunctional Synergy to Promote Healing of Infected Wounds

Xiaoqiang Wang[1,*], Kai Zhu[1,*], Wanxin Liu[1,*], Guoying Deng[2], Yuanyuan Peng[1], Haiming Lu[1], Qiugen Wang[1]

[1]Department of Orthopedics, Yueyang Hospital of Integrated Traditional Chinese and Western Medicine, Shanghai University of Traditional Chinese Medicine, Shanghai, 200437, People's Republic of China; [2]Trauma Center, Shanghai General Hospital, Shanghai Jiao Tong University School of Medicine, Shanghai, 201620, People's Republic of China

*These authors contributed equally to this work

Correspondence: Qiugen Wang; Haiming Lu, Department of Orthopedics, Yueyang Hospital of Integrated Traditional Chinese and Western Medicine, Shanghai University of Traditional Chinese Medicine, Shanghai, 200437, People's Republic of China, Email wangqiugen@126.com; luhaiming78@163.com

Introduction: The management of chronic infected wounds imposes a substantial economic burden on patients and significantly impairs their quality of life due to persistent wound infections and delayed healing. To address this issue, we developed a multifunctional dressing with sustained hydrogen sulfide (H_2S) release to accelerate wound healing.

Methods: Sodium hydrosulfide-loaded cerium oxide (NaSH@CeO_2) was synthesized via rotary evaporation and subsequently incorporated into a hydrogel dressing crosslinked with chitosan (CS) and hyaluronic acid (HA), yielding NaSH@CeO_2/CS-HA. The composite was characterized, and H_2S release was quantified using the methylene blue method. The biological functions of NaSH@CeO_2/CS-HA were evaluated through CCK-8 assay, Calcein-PI staining, DCFH-DA detection, scratch assay, tube formation assay, and antibacterial tests. A methicillin-resistant *Staphylococcus aureus* (MRSA)-infected wound model was established in rats to assess therapeutic efficacy based on wound healing rate, hematoxylin-eosin (H&E) staining, Masson's trichrome staining, and immunofluorescence staining.

Results: NaSH@CeO_2/CS-HA demonstrated sustained H_2S release without cytotoxicity while effectively inhibiting *Escherichia coli* and MRSA. Furthermore, it reduced intracellular reactive oxygen species levels, maintained cell viability under H_2O_2-induced oxidative stress, promoted mouse fibroblast cells (L929 cells) migration, and enhanced tube formation in human umbilical vein endothelial cells (HUVECs). In the MRSA-infected rat wound model, the NaSH@CeO_2/CS-HA group achieved a 98.1% wound closure rate by day 14. H&E and Masson's staining revealed enhanced tissue healing, while immunofluorescence (CD31, Caspase-3) confirmed increased angiogenesis and reduced apoptosis at the wound site.

Conclusion: The developed gel dressing (NaSH@CeO_2/CS-HA) intelligently regulates H_2S release, combining antioxidant, antibacterial, and wound-healing functions into one, providing a comprehensive treatment solution for chronic infectious wounds with significant clinical application potential.

Keywords: wound healing, MRSA infected wound, hydrogen sulfide, cerium oxide nanoparticle, hydrogel

Introduction

The skin, the largest organ of the human body, possesses a robust self-healing ability.[1] However, deep wounds and large defects necessitate complex treatments for complete healing. Without appropriate care, these conditions may lead to persistent acute and chronic health issues.[2,3] Acute wounds usually heal in 5 to 10 days, or up to 30 days after the injury. However, chronic wounds do not heal after 12 weeks from the initial injury.[4] For acute wounds, existing wound dressings

https://doi.org/10.2147/IJN.S538774
Received: 6 May 2025
Accepted: 2 February 2026
Published: 3 March 2026

Graphical Abstract

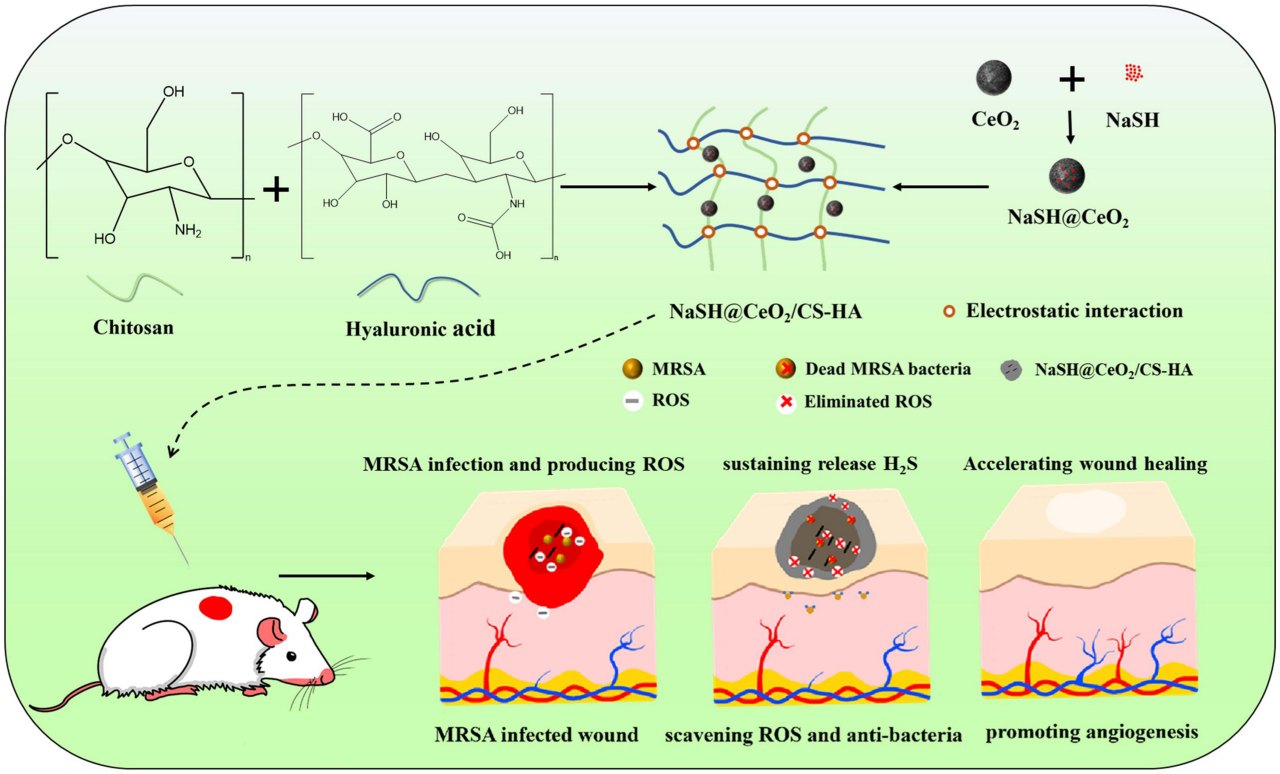

have demonstrated preliminary effectiveness. They create a breathable and moist wound environment, which can effectively promote wound healing.[5] However, chronic wounds are difficult to heal due to factors such as infection, ischemia, and excessive collagen degradation, rendering traditional treatment methods such as gauze bandaging, skin grafting, and even skin flap transplantation ineffective, which places a significant social, economic, and quality of life burden on patients.[6–9]

Chronic wounds are difficult to heal primarily due to the excessive accumulation of reactive oxygen species (ROS) and an increased susceptibility to bacterial infections.[10,11] Persistent wounds maintain an environment where inflammatory cells, such as neutrophils and macrophages, continuously exist.[12] This condition leads to excessive production of ROS, which in turn activates cellular signaling pathways that interfere with angiogenesis, thereby delaying the healing process.[13] Moreover, persistent skin wounds disrupt the skin's innate protective functions, making it susceptible to bacterial infections.[14] The colonization and proliferation of bacteria in these wounds trigger intense inflammatory responses, leading to high levels of ROS. This excessive ROS production damages skin oxygenation and nutrition,[15] impeding wound healing and potentially causing severe systemic reactions.[16] Chronic infection and oxidative stress (OS) damage mutually reinforce each other, ultimately leading to the prolonged non-healing of wounds.[17] Therefore, the main approaches to treating infected wounds healing involve controlling infection, reducing OS damage, and promoting wound healing.[18]

The application of hydrogen sulfide (H_2S) in wound treatment has recently become a research focus in the field of burn and trauma medicine.[19] H_2S, an endogenous gas neurotransmitter, exhibits several biological effects, including anti-inflammatory, antioxidant, and cell proliferation-promoting properties, which are crucial for wound healing.[20] H_2S can regulate the activity of macrophages and reduce the release of inflammatory cytokines, thereby alleviating the inflammatory response.[21] Additionally, it can activate intracellular signaling pathways in cells, such as the ERK/MAPK pathway, to promote cell proliferation and migration.[22,23] Furthermore, its significant antioxidant properties help

eliminate excessive free radicals produced during the healing process, protecting cells from OS damage.[24] H_2S can also promote the secretion of endothelial growth factors, stimulate the formation of new blood vessels, and provide sufficient oxygen and nutrients for wound healing.[25,26] Since skin wounds often show a deficiency in endogenous H_2S,[27] exogenous supplementation has proven effective in treatment. The drug ATB-346, which releases exogenous H_2S, has entered clinical trials, demonstrating the clinical translational potential of exogenous H_2S-releasing drugs.[28] In conclusion, slowly releasing H2S gas onto wounds represents a promising treatment strategy for chronic wounds because it offers a smart-enhanced therapeutic approach that can promote wound healing, potentially through mechanisms like stimulating angiogenesis, reducing inflammation, and accelerating cell migration.[29]

Sodium hydrosulfide (NaSH) is widely recognized as the most common H_2S donor, known for its ability to rapidly increase H_2S concentrations.[30] However, its poor stability in biological environments poses challenges in controlling the precise dosage of H_2S.[31] When H_2S levels are too low, the therapeutic benefits are reduced, making it difficult to maintain an effective concentration at wound sites.[32] Conversely, excessively high levels can lead to toxicity, which restricts the practical use of NaSH in wound treatment.[33]

Current strategies often involve the physical loading of H_2S donors (such as NaSH) into hydrogels or microspheres.[34] However, these systems commonly suffer from burst release, inability to respond to the pathological microenvironment, and limited functionality, which may lead to local toxicity and restricted therapeutic efficacy.[35,36] Hollow mesoporous cerium dioxide nanoparticles (CeO_2-NPs), are regarded as excellent drug carriers due to their high specific surface area and pore volume.[37] Nevertheless, in this study, we did not simply treat them as inert containers. Instead, we strategically leveraged the intrinsic physicochemical properties of CeO_2-NPs to transform them from passive carriers into active "regulators" and "synergistic therapeutic agents", thereby constructing an intelligent H_2S delivery system.

The hollow shell of CeO_2 constitutes a physical barrier that effectively delays the diffusion of NaSH, thereby achieving a fundamental sustained-release function.[38] More importantly, CeO_2 exhibits responsiveness to the weakly acidic microenvironment of wounds (pH 6.5–7.0). Under acidic conditions, changes in the surface potential of CeO_2 and its slight dissolution behavior intelligently accelerate the release of H_2S, enabling targeted treatment in the most severely infected regions with the lowest pH.[39] Furthermore, the unique Ce^{3+}/Ce^{4+} cycling endows CeO_2 not only with the ability to catalyze the generation of H_2S, but also to consume detrimental ROS, thereby indirectly "protecting" H_2S, prolonging its half-life, and ensuring its effective bioavailability.[40–42] This strategy of modulating gas release kinetics through microenvironmental regulation cannot be achieved by simple carriers.

CeO_2-NPs possess unique pH-dependent nanozyme activity. Under neutral pH conditions, they primarily exhibit ROS scavenging activity, which protects healthy tissues.[43] In contrast, within acidic infectious microenvironments, they demonstrate significant peroxidase-like activity, catalyzing the conversion of endogenous H_2O_2 into highly toxic hydroxyl radicals (·OH), thereby specifically eliminating bacteria.[44,45] This "smart switching" characteristic makes CeO_2-NPs an ideal microenvironment-responsive antibacterial agent. Compared to traditional bactericidal agents such as silver nanoparticles, CeO_2-based systems exert precise and on-demand antibacterial effects. While performing antibacterial functions, CeO_2 also effectively alleviates OS at the wound site through its ROS scavenging capability, creating an anti-inflammatory and pro-healing microenvironment. In combination with the pro-angiogenic function of H_2S gas, it collectively accelerates the healing of infected wounds.

In our research, we prepared porous CeO_2-NPs encapsulating NaSH. This achieved multiple effects, including antibacterial activity, antioxidant stress resistance, and promotion of angiogenesis. Notably, CeO_2-NPs tend to aggregate into larger particles in aqueous solutions, which can affect their biological behavior.[46] Therefore, the selection of an appropriate medium is crucial. Chitosan (CS), a natural cationic polysaccharide, offers excellent biocompatibility and biodegradability.[47] Hyaluronate (HA), a natural high-molecular-weight polymer, also exhibits good biocompatibility. It has additional properties such as anti-aging, anti-inflammatory effects, and hydration.[48] HA molecules have numerous hydroxyl groups that can bind to amino groups on protonated CS chains via electrostatic interactions, forming a physically cross-linked hydrogel with self-healing properties and drug release capabilities.[49,50] This hydrogel ensures the stable distribution of CeO_2 and the slow release of H_2S. CS-HA, as a biocompatible hydrogel, can seal wounds, maintain a moist wound environment, absorb tissue exudates, reduce inflammation, and allow gas exchange.[51] Compared to traditional wound dressings like gauze, it provides better isolation from external microorganisms.[52]

Therefore, our study successfully developed an intelligent NaSH delivery system (NaSH@CeO_2) based on hollow CeO_2-NPs and embedded it into a hydrogel for ease of application. This system not only achieved sustained and microenvironment-responsive release of H_2S, but also enabled intelligent regulation of H_2S release kinetics and synergistic enhancement of multiple biological functions through the interaction between the carrier and the drug. Our study demonstrate that this integrated strategy offers a promising novel approach for the treatment of complex, refractory infected wounds.

Materials and Methods

Materials

NaSH, Ce $(NO_3)_3 \cdot 6H_2O$, CS, sodium hyaluronate and phosphate-buffered saline (PBS) were sourced from Macklin (Shanghai, China). Acetic acid, ethylene glycol was obtained from Sinopharm Chemical Reagent (Shanghai, China). Cell Counting Kit-8 (CCK-8) assay reagent, Calcein-AM/PI assay, DCFH-DA assay kit reagent, Matrigel Matrix, methylene blue and simulated body fluid (SBF) were acquired from Yeason (Shanghai, China). Primary human umbilical vein endothelial cells (HUVECs, <8 passages), L-929 Mouse Fibroblast Cell (L929 cells, <8 passages), endothelial cell medium (ECM), Dulbecco's Modified Eagle Medium/Nutrient Mixture F-12 (DF-12), fetal bovine serum, antibiotic solution and endothelial cell growth supplement were obtained from ScienCell (California, USA). Methicillin-resistant Staphylococcus aureus (MRSA, ATCC 43300) and E. coli (ATCC 25922) were derived from ATCC (Manassas, USA). 4% paraformaldehyde was acquired from Beyotime Biotechnology (Shanghai, China).

X-ray diffraction (XRD) was performed using a D8 Advance Da Vinci instrument (USA). Transmission electron microscopy (TEM) was conducted using a JEM-2100F microscope (JEOL, Japan). Fourier transform infrared spectroscopy (FTIR) was carried out using a PerkinElmer Spectrum instrument.microplate reader (Thermo Fisher Scientific, USA).

Fabrication and Characterization of NaSH@CeO_2/CS-HA

Synthesis of Porous CeO_2-NPs

Firstly, 1 g of Ce $(NO_3)_3 \cdot 6H_2O$ was dissolved in 1 mL of deionized water. Then, 1 mL of acetic acid (ethanoic acid) and 30 mL of ethylene glycol were added to this solution, followed by stirring for 30 minutes. Subsequently, the resulting mixture was then transferred to a hydrothermal reactor and heated at 180 °C for 150 minutes. Finally, the product was washed three times with ethanol.

Synthesis of NaSH@CeO_2/CS-HA, CeO_2/CS-HA, or CS-HA

Dissolve 10 mg of CeO2-NPs and 1 mg of NaSH in deionized water and mix thoroughly. The water was removed using spin distillation to obtain NaSH@CeO_2. Chitosan (200 mg) was dissolved in 10 mL of 0.75% acetic acid solution. After complete dissolution, NaSH@CeO_2 was added and then mixed thoroughly. Subsequently, 200 mg of sodium hyaluronate was added and the mixture was stirred for 2–3 hours. No NaSH was added during the synthesis of CeO_2/CS-HA. For CS-HA, neither CeO_2-NPs nor NaSH were added.

Apparent Adhesion of NaSH@CeO_2/CS-HA

Directly attach the hydrogel sheet to the surface of various substrates and use a vertical pull method to visually demonstrate the adhesive properties of the gel.

Compression Test of NaSH@CeO_2/CS-HA and CS-HA

Cut off the cap and bottom of a 5 mL centrifuge tube and place it in a 24-well plate. Place 1 mL of the gel on a universal testing machine to test its compressive properties. The gel has a diameter of 12 mm, a base area of 1809.6 mm^2, and its height is measured precisely using a Vernier caliper. Enter the gel parameters into the universal testing machine and start the compression test. After the test, the compressive modulus of the gel is obtained. Each sample is tested in triplicate.

Nitrogen Adsorption-Desorption Testing of Hollow CeO_2-NPs

The specific surface area and pore structure of the as-synthesized hollow CeO_2 nanoparticles were characterized by N_2 adsorption-desorption measurements at 77 K using a Micromeritics ASAP 2460 surface area and porosity analyzer. Prior to the analysis, the sample was degassed under vacuum at 120 °C for 6 h to remove any adsorbed impurities. The specific surface area was calculated from the adsorption data in the relative pressure (P/P_0) range of 0.05–0.30 using the Brunauer-Emmett-Teller (BET) method. The pore size distribution and pore volume were derived from the desorption branch of the isotherm using the Barrett-Joyner-Halenda (BJH) model.

Release Profile of H_2S

The release of H_2S was determined using methylene blue as an indicator.[34] The release profile of H_2S from NaSH@CeO_2/CS-HA was measured in the SBF at pH levels of 6.5, 7.4 and 9.1 mL of NaSH@CeO_2/CS-HA was incubated in 5 mL SBF solution under shaking (40 rpm) at 37 °C. At the specific time intervals, 100 μL of SBF solution and 1% zinc acetate (100 μL) were added to a pre-mixed solution that containing $FeCl_3$ (30 mM in 1.2 M HCl, 20 μL) and DMPD (20 mM in 7.2 M HCl, 20 μL). After incubation 20 minutes at room temperature, the optical absorbance of the resulting solution was measured at 670 nm using a microplate reader. The experiment was conducted in triplicate and at each around, 100 μL fresh SBF solution was replaced to establish the sink condition.

In vitro Antibacterial Activity of NaSH@CeO_2/CS-HA

To assess the broad-spectrum antibacterial effect of the hydrogel dressing, Gram-positive MRSA and E. coli were cultured. Luria-Bertani (LB) broth was used to resuspend logarithmic-phase bacterial cells, achieving a final cell density of 1×10^6 colony-forming units per milliliter (CFU/mL). The hydrogel samples (CS-HA, CeO_2/CS-HA, and NaSH@CeO_2/CS-HA) were then incubated with 2 mL of bacterial suspension. After 12 hours, a 100 μL volume of bacterial droplets was evenly distributed onto the center of a LB agar plate to determine the colony count. The antibacterial capacity of the nanoparticles was evaluated based on the colony counts after 24 hours.

Cell Cultures and Cytocompatibility

L929 cells were cultured in DF-12 medium supplemented with 5% fetal bovine serum, 1% antibiotic solution, and 1% antifungal solution; HUVECs were cultured in ECM, supplemented with 5% fetal bovine serum, 1% antibiotic solution, and 1% endothelial cell growth supplement. The cytocompatibility of dressings was assessed using CCK-8 and Calcein-PI assays.

CCK-8 Assay

Initially, L929 cells and HUVECs were seeded at a density of 5000 cells per well in a 96-well plate. After 24 hours, the culture medium was replaced with NaSH@CeO_2, at varying concentrations ranging from 10 to 1000 μg/mL. Subsequently, after 24 hours of incubation, CCK-8 solution (10 μL) was added, and absorbance was measured at 450 nm.

Calcein-PI Staining

L929 cells were seeded at 50,000 cells/mL in a 12-well plate. After overnight culture, the medium was replaced with 2 mL of fresh complete DF-12 medium. Concurrently, blank CS-HA hydrogel, CeO_2/CS-HA and NaSH@CeO_2/CS-HA were gently placed on top of the cells respectively. Cells without any treatment were used as negative controls. Cells without any treatment served as negative controls. After a specified period, the cell viability was analyzed using Calcein-AM/PI staining solution, and fluorescence microscopy was employed to observe cell viability.

Antioxidant Activity of NaSH@CeO_2/CS-HA

DCFH-DA Assay

To assess intracellular ROS levels, L929 cells were cultured in a 12-well plate. After 24 hours, the culture medium was replaced with fresh DF-12 medium for the following groups: control group (1 mL), OS group (H_2O_2), OS group with CS-

HA (H_2O_2 + CS-HA), and OS group with NaSH@CeO_2/CS-HA (H_2O_2 + NaSH@CeO_2/CS-HA). In the OS group, 600 μmol/L H_2O_2 was added. After a specified period, the DCFH-DA assay kit was used to detect intracellular ROS. Cells were gently washed with PBS, followed by the addition of the DCFH-DA probe. After 30 minutes of incubation at 37 °C in the dark, fluorescence microscopy (excitation = 488 nm, emission = 520 nm) was employed to quantify ROS levels using Image J software.

Calcein-PI Staining Under OS

To evaluate the protective effect of the hydrogel under OS, L929 cells were seeded at a density of 50,000 cells/mL. The procedure was similar to the DCFH-DA staining. After washing with PBS, Calcein-AM/PI staining solution was added to each well. After 30 minutes of incubation at 37°C in the dark, cells were observed using fluorescence microscopy. Channels: Calcein-AM (excitation = 494 nm, emission = 517 nm), PI (excitation = 535 nm, emission = 617 nm).

Cell Migration

To study the wound healing potential of NaSH@CeO_2/CS-HA, an in vitro wound model was established using L929 cells and HUVECs. Cells were seeded at 100,000 cells/mL in a 6-well plate. After 24 hours, the culture medium was replaced with serum-free medium to inhibit cell proliferation, ensuring that wound closure was solely due to cell migration. A fine scratch was made at the bottom of each well using a sterile pipette tip, followed by two PBS washes to remove debris. The control group received serum-free culture medium, while treatment groups included CS-HA, CeO_2/CS-HA, and NaSH@CeO_2/CS-HA. Image J software was used to analyze wound closure based on the proportion of migrated cells filling the wound area at 0 and 24 hours.

Tube Formation Assays

To simulate vascular formation under H_2O_2-induced injury, Matrigel Matrix was coated in each well of a 24-well cell culture plate (200 μL/well) and allowed to solidify at 37 °C for 30 minutes. HUVECs were then seeded on the Matrigel-coated plate. The same procedure as the intracellular ROS experiment was followed. After 12 hours of incubation, tube formation was observed using a microscope, and Image J software was used to measure the number of junctions and branches in each field. Three random fields were analyzed per well.

Wound and Infection Model

Male SD rats weighing 150 ± 10 g were used for in vivo experiments (n=24). All animal procedures followed guidelines set by the Shanghai Experimental Animal Accreditation Committee and were approved by the Institutional Review Board of Shanghai First People's Hospital (IACUC number: 2024AWS468). Rats were anesthetized with Zoletil®50 (50 mg/kg, intramuscular injection). Circular full-thickness skin defects (diameter: 10.0 mm) were created on the rat dorsum. The wounds were infected with 20.0 μL of MRSA bacterial suspension (1×10^8 CFU/mL).

Wound Closure Evaluation

SD rats were anesthetized with Zoletil®50. After 75% ethanol disinfection, circular full-thickness skin wounds (diameter: 10.0 mm) were created in the middle of the rat dorsum using a biopsy punch. Dressings were changed every other day, and wound healing was documented using a digital camera at 4 days, 7 days, 10 days, and 14 days. On the fourteenth day, wound area measurements were captured using Image J software after calibration.

Histological and Immunohistochemistry Analyses

Euthanasia was performed using carbon dioxide asphyxiation on SD rats. Day 14 skin specimens were immediately collected, washed in water, fixed in 4% paraformaldehyde, embedded in paraffin, and sectioned (4 μm thickness). Subsequently, sections were stained with hematoxylin and eosin (H&E) and Masson's trichrome stain according to the manufacturer's instructions. H&E staining was used to assess tissue morphology and scar width. Masson's trichrome staining evaluated collagen density and number of new vessels in the regenerative area. Image J software was employed for image analysis.

Immunofluorescence staining was performed to assess CD31 and caspase-3 levels on the 7th day. Briefly, after fixation in 4% paraformaldehyde and permeabilization with 0.2% Triton X-100, samples were blocked with 5% bovine serum albumin (BSA) in PBS. Primary antibodies were incubated overnight at 4°C. After PBS washing, samples were exposed to fluorescent-labeled secondary antibodies for 1 hour. Image J software was used for image processing, averaging results from at least three randomly selected positions.

Statistical Analyses

All experiments were repeated three times (n = 3), and quantitative data are presented as mean ± standard deviation for 3–5 samples per group. Statistical comparisons between groups and the control group were performed using ANOVA. p -value < 0.05 indicated statistically significant differences: * $p < 0.05$; ** $p < 0.01$; *** $p < 0.001$.

Results

Material Characterization

Characterizations of the NaSH@CeO_2/CS-HA Hydrogel

Figure 1 presents the structural characteristics of the samples. Optical photographs of NaSH@CeO_2/CS-HA are depicted in Figure 1a. The addition of HA transforms the simple CS from a solution state to a gel-like structure, signifying a gradual and uniform cross-linking process facilitated by CS-HA cross-linking agent.

The morphologies of CeO_2-NPs were examined using TEM (Figure 1b). The study reveals that the porous CeO_2-NPs have a uniform pore size distribution, with an average size ranging from 50 to 120 nm. The surface of CeO_2-NPs exhibits numerous active sites, providing ample anchor points for the in-situ growth of NaSH. Figure 1c, reveal that the NaSH@CeO_2/CS-HA hydrogel exhibits a typical three-dimensional porous structure. This structure facilitated the release of substances, the adhesion of cells, and the transportation of nutrients, making it an ideal wound dressing. It successfully incorporates porous CeO_2-NPs loaded with NaSH.

The Figure 1d displays the FTIR spectra at different synthesis stages, demonstrating successful material synthesis. The absorption peak at 800 cm^{-1} is attributed to the Ce-O bond, which belongs to the crystalline nCeO_2 active phonon mode and ranges from 900 cm^{-1} to 400 cm^{-1}. 1000 ~ 1200 cm^{-1} represents the C-O-C stretching vibration peak, the characteristic peak of CS;[53] The symmetric stretching vibration of double bond C=O (amide I band) and the characteristic peaks of carboxyl group at 1,500 ~ 1,680 $cm^{-1}$and 1,380 $^{-1}$500 cm^{-1} are the characteristic peaks of HA.[54] In each group, strong and wide absorption peaks existed at 3,000 ~ 3,750 cm^{-1}, which generally corresponded to O-H and N-H stretching vibrations, indicating that ionic bonds form between CS polycations and HA polyanions. In summary, CS and HA form hydrogels through electrostatic interaction.

Slow Release of H_2S

Figure 1e–g illustrates the release profile of H_2S from NaSH@CeO_2/CS-HA hydrogel. At pH 9, the amount of H_2 S released within 2 hours was significantly lower than that measured at pH 6.5 and pH 7.4. This performance is significantly superior to the direct use of NaSH. It indicates that the NaSH@CeO_2/CS-HA hydrogel effectively controls the release of H_2S, making it a promising material for various applications.[34]

Mechanical Property of the NaSH@CeO_2/CS-HA Hydrogel

The NaSH@CeO_2/CS–HA hydrogel exhibited favorable adhesion to PE, rubber, and PP, as visually demonstrated in the apparent adhesion images (Figure 1h). As shown in the compressive modulus diagram (Figure 1i), the incorporation of NaSH@CeO_2 did not alter the mechanical strength of the CS–HA matrix, as both hydrogels exhibited similar modulus values (approximately 0.03 kPa) with no significant differences observed.

Nitrogen Adsorption-Desorption Testing of Hollow CeO_2-NPs

As shown in Figure 1j, the N_2 adsorption–desorption isotherm of CeO_2 exhibits a typical type IV pattern, confirming the presence of a highly ordered mesoporous structure. The BJH pore size distribution curve displays a very sharp and narrow peak (full width at half maximum <1 nm), with an average pore size of 3.402 nm. More importantly, the material demonstrates a high specific surface area of 310.252 $m^2 \cdot g^{-1}$.

 https://doi.org/10.2147/IJN.S538774

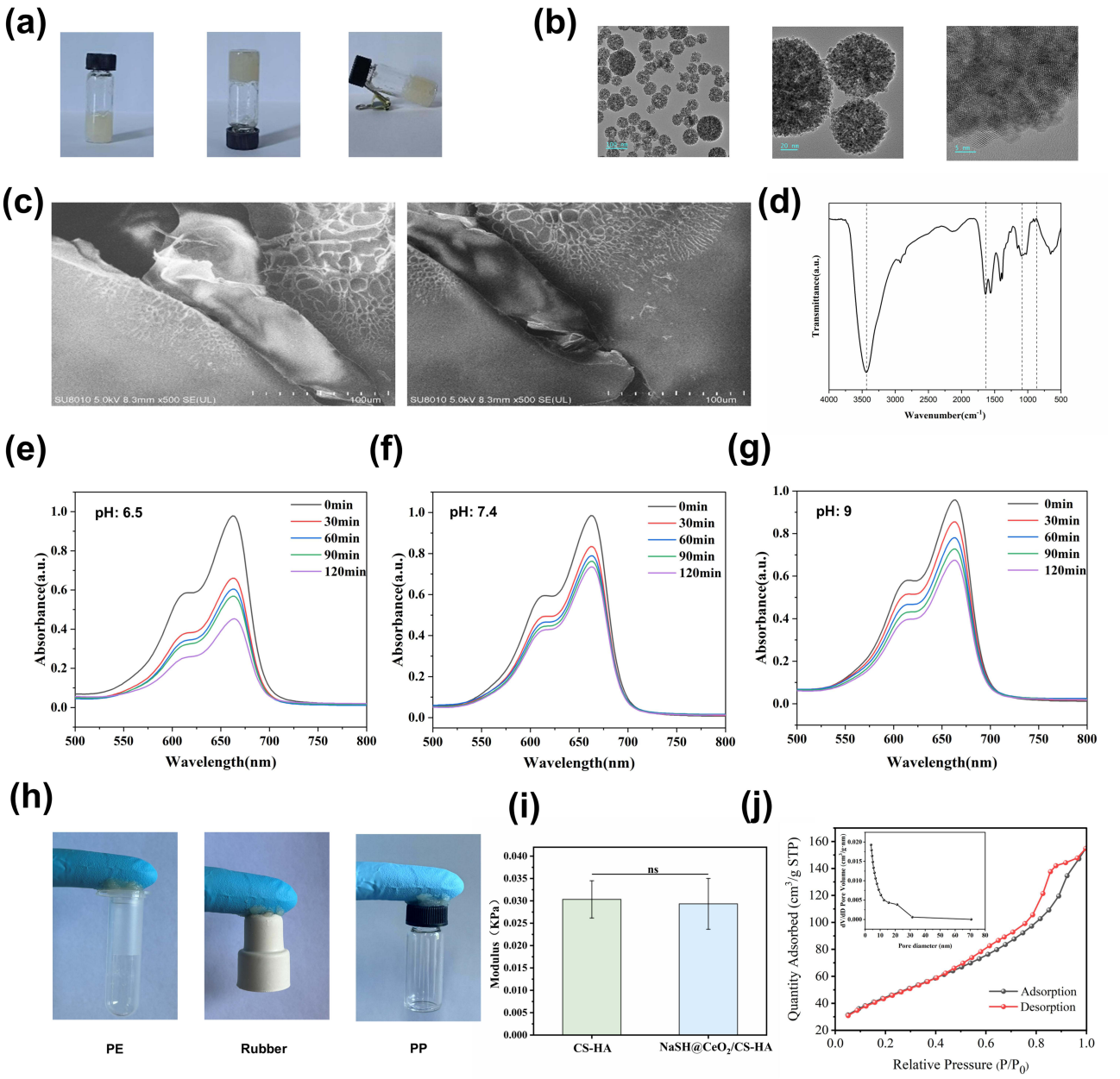

Figure 1 Characterizations of the material. (**a**) Optical photographs of NaSH@CeO_2/CS-HA. (**b**) The appearance of CeO_2 at different magnifications was collected by TEM, and irregular porous structure could be seen on the sample surface. The scale bar represents 100 μm, 20 μm and 5 μm. (**c**) The appearance of CS-HA at different magnifications was collected by SEM. (**d**) The FTIR spectra of NaSH@CeO_2/CS-HA materials. (**e**–**g**) Accumulated amount of H_2S released from NaSH@CeO_2/CS-HA at different time points in different pH environments. (**h**) Apparent adhesion of NaSH@CeO_2/CS-HA hydrogel. (**i**) Compressive modulus of CS-HA and NaSH@CeO_2/CS-HA hydrogel. (**j**) Nitrogen adsorption-desorption isotherms and pore size distribution of hollow CeO_2-NPs. (ns: no significant difference).

Evaluation of Biocompatibility of NaSH@CeO_2/CS-HA Hydrogel

Histocompatibility of NaSH@CeO_2/CS-HA Hydrogel

The liver and kidneys play crucial roles in metabolism, detoxification, and excretion within the body. Given that these organs are major sites for nanoparticle accumulation, it is essential to assess the histocompatibility of the NaSH@CeO2/CS-HA hydrogel with liver and kidney tissues.[55,56] After treatment with NaSH@CeO_2/CS-HA, histological examination after 2 weeks revealed no significant differences compared to normal tissue structures in Figure 2a.

https://doi.org/10.2147/IJN.S538774

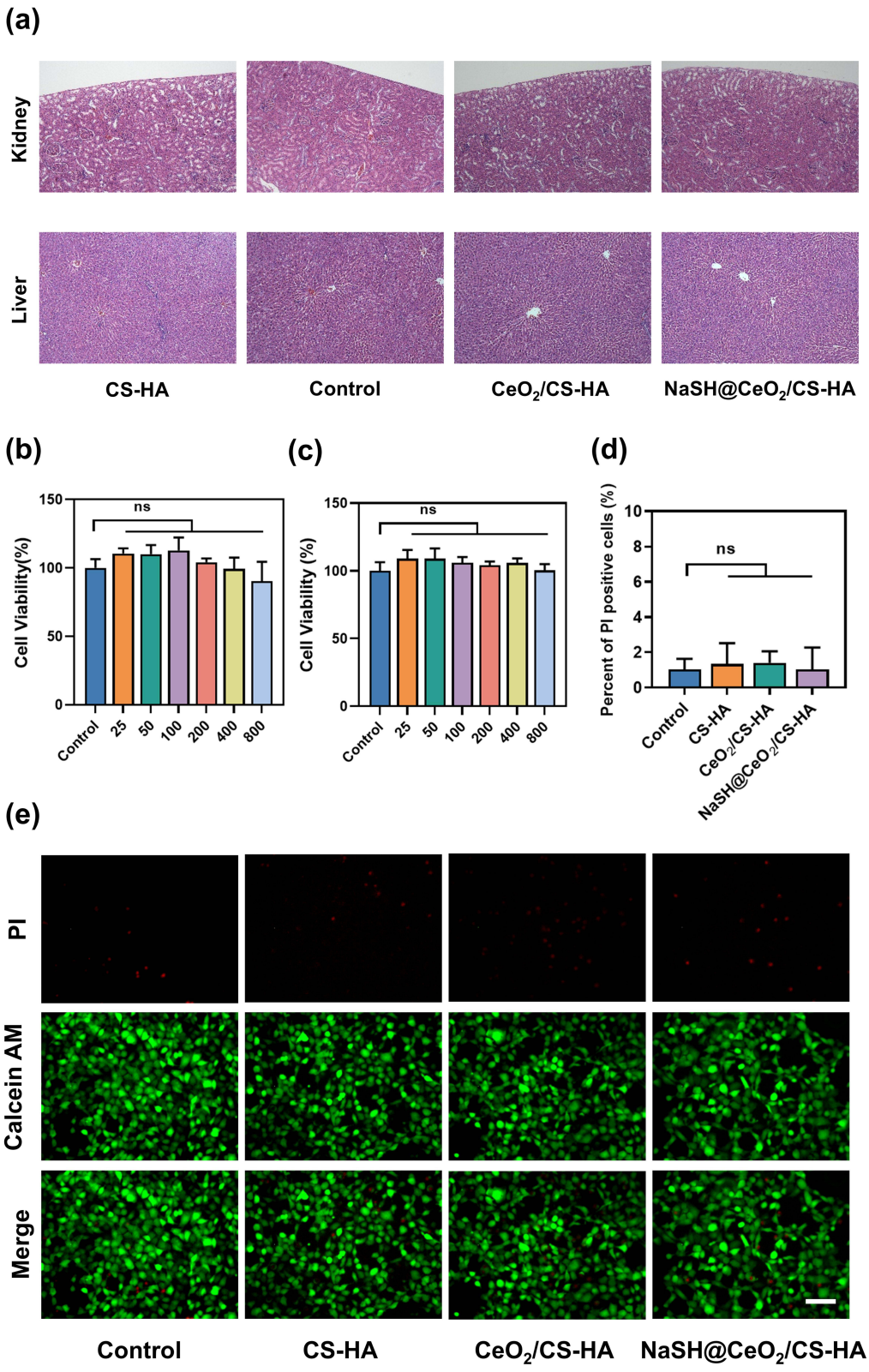

Figure 2 The histocompatibility and cytocompatibility of NaSH@CeO_2/CS-HA. (**a**) After 2 weeks of NaSH@CeO_2/CS-HA implantation, no significant inflammation or immune rejection response in the liver and the kidney, indicating great histocompatibility. The scale bar represents 100 μm. The HUVECs (**b**) and L929 cells (**c**) cytocompatibility of NaSH@CeO_2/CS-HA were detected using CCK-8 assay, and L929 cells were tested for Calcein-AM/PI assay (**d** and **e**). The scale bar represents 50 μm. The data represents the mean ± SD, and experiments were conducted with three repetitions. (ns: no significant difference).

https://doi.org/10.2147/IJN.S538774

Cytocompatibility of NaSH@CeO_2/CS-HA Hydrogel

When applied to wounds, dressings must exhibit good cell compatibility to avoid inducing toxicity around the wound area and impeding wound healing.[57] The CCK-8 assay was utilized to assess the cytocompatibility of NaSH@CeO_2/CS-HA. As shown in Figure 2b and c, different concentrations of NaSH@CeO_2 led to cell viability exceeding 100% in HUVECs and L929 cells, indicating no significant cytotoxicity. Figure 2d demonstrated that both the experimental group (treated with CS-HA, CeO_2/CS-HA and NaSH@CeO_2/CS-HA) and the control group exhibited minimal PI-positive cells, with a proportion of PI-positive cells less than 5%. Statistical analysis presented in Figure 2e revealed no significant difference between the control and experimental groups, indicating comparable cell viability. Overall, NaSH@CeO_2/CS-HA demonstrated excellent cytocompatibility, providing a favorable environment for cell survival in wound settings.

Evaluation of the Antibacterial Activity of NaSH@CeO_2/CS-HA Hydrogel

Chronic wound healing delays often lead to bacterial infections.[58] With the overuse of antibiotics, the incidence of drug-resistant bacterial infections is increasing, and ideal treatment options are often lacking. Among these drug-resistant bacteria, MRSA, a common Gram-positive bacterium, and E. coli, a Gram-negative bacterium, are frequently associated with wound infections.[59]

To evaluate the antibacterial activity, the agar plate method was employed to test the inhibitory effects of CS-HA, CeO_2/CS-HA and NaSH@CeO_2/CS-HA. As shown in Figure 3a–c, the results demonstrated that NaSH@CeO_2/CS-HA exhibited antibacterial properties against both E. coli and MRSA.

In vitro ROS-Scavenging

Excessive OS plays a significant role in delaying wound healing.[60] Therefore, dressings for chronic infected wounds should address OS and protect cells from damage caused by excessive ROS.[61]

We investigated the ability of NaSH@CeO_2/CS-HA to prevent cell death related to OS. When L929 cells were exposed to 300 μmol/L H_2O_2, PI staining revealed 43.4% cell death. However, pretreatment of L929 cells with therapeutic concentrations of NaSH@CeO_2/CS-HA resulted in a cell death rate of 5.9% (Figure 4a and b), demonstrating the cell-protective effect of NaSH@CeO_2/CS-HA under OS conditions.

To assess whether NaSH@CeO_2/CS-HA achieves cell protection by reducing intracellular ROS, we used the DCFH-DA probe. After H_2O_2 treatment, L929 cells exhibited significantly elevated ROS levels. In contrast, NaSH@CeO_2/CS-HA-pretreated cells showed significantly reduced intracellular ROS levels compared to untreated control cells, while CS-HA alone did not reduce ROS levels (Figure 4c and d). This confirms that NaSH@CeO_2/CS-HA can reduce intracellular ROS levels in an OS environment, providing effective cell protection.

In-vitro Scratch Assay

Cell migration toward the injured site is crucial for wound healing. Previous research has demonstrated that hydrogels, including non-gelling materials, promote wound repair both in vitro and in vivo.[62] In this study, we assessed the migration capacity of fibroblasts and vascular endothelial cells to the injured area to determine the wound healing trend. The results (Figure 4e and f) revealed that 24 hours after treatment, the cell migration coverage gap was 59.06% for L929 cells pretreated with NaSH@CeO_2/CS-HA. In contrast, fibroblast migration was slower in the CS-HA (30.35%) and CeO_2/CS-HA (36.68%) groups, with no significant difference compared to the control group (27.3%). Notably, the cell migration-promoting effect of NaSH@CeO_2/CS-HA was significantly higher than that of other groups. As shown in Figure 4g and h, a similar trend was observed in HUVECs, with a significant increase in cell migration in the NaSH@CeO_2/CS-HA group, accounting for 64.74%. These findings suggest that the sustained release of H_2S from the nanoscale formulation loaded with NaSH enhances cell migration and proliferation, potentially contributing to wound healing.

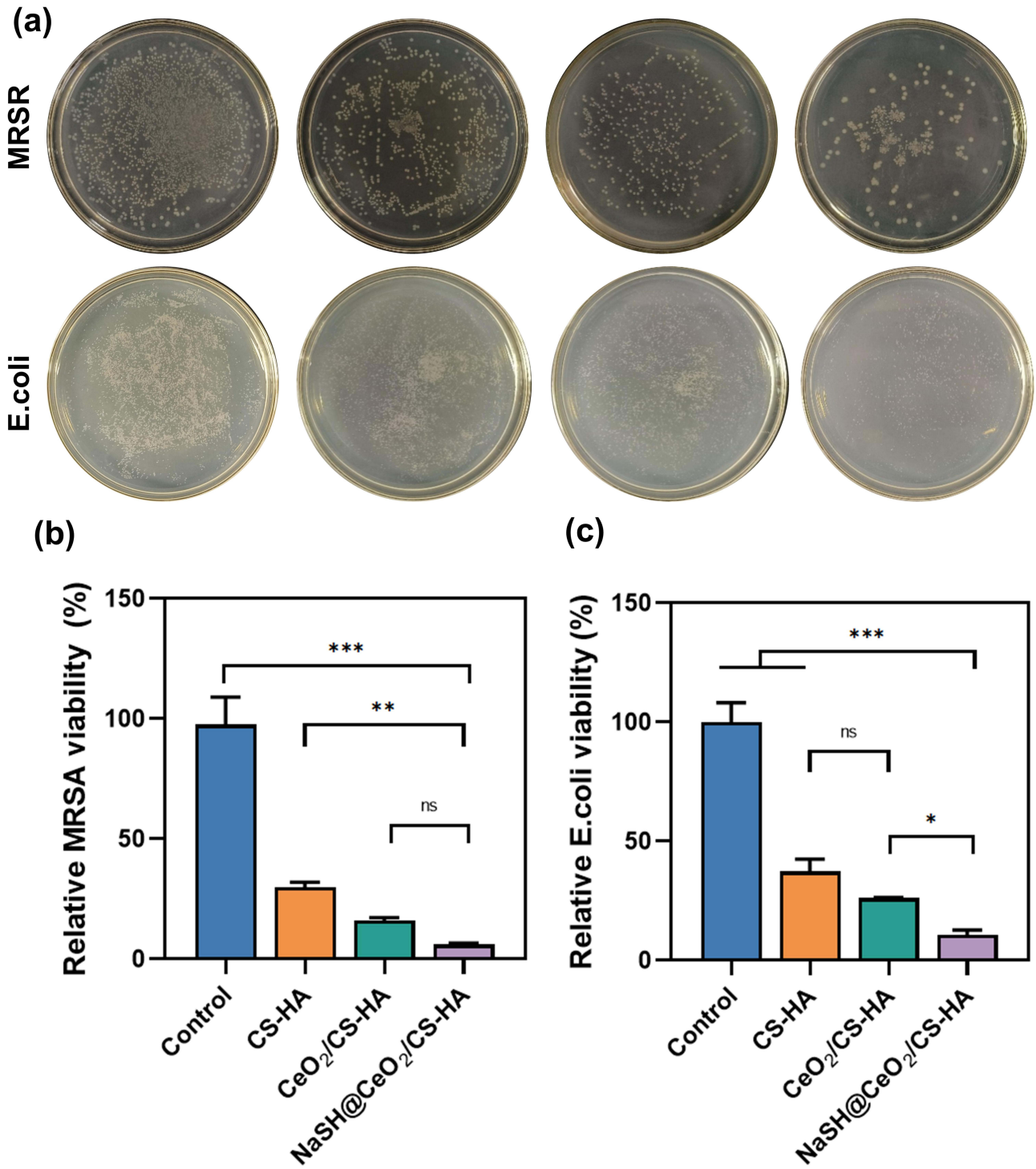

Figure 3 Antibacterial efficacy of different materials. (**a**) Survival of E. coli and S. aureus after the treatment with PBS, CS-HA, CeO_2/CS-HA, and NaSH@CeO_2/CS-HA were assessed and presented, and the viability of MRSA (**b**) and E. coli (**c**) was measured. NaSH@CeO_2/CS-HA exhibited significant antibacterial activity against both E. coli and MRSA. The data represents the mean ± SD. (*$p < 0.05$, ** $p < 0.01$, *** $p < 0.001$, ns: no significant difference).

In-vitro Tube Formation Assay

Excessive OS in infected wounds disrupts blood vessel formation and hinders wound healing.[63] To address this, we developed a model to evaluate the angiogenic capacity of HUVECs under simulated OS conditions. When exposed to OS conditions, HUVECs (Figure 4i–k) pretreated with NaSH@CeO_2/CS-HA exhibited a protective effect, maintaining the

https://doi.org/10.2147/IJN.S538774

number of junction and branches similar to the control group (without OS). Moreover, the NaSH@CeO_2/CS-HA-treated cells showed a significant increase in the number of junction and branches compared with other OS induced groups, suggesting that he controlled release H_2S from the nanoscale formulation loaded with NaSH enhances blood vessel formation under OS conditions.

NaSH@CeO_2/CS-HA Promotes Infection Wounds Healing in the Rat Models

The NaSH@CeO_2/CS-HA hydrogel was evaluated for its accelerated effect on wound healing in an MRSA-infected rat full-thickness skin incision model. Representative photos, schematic diagrams and wound closures of the treated wounds at each time point are shown in the Figure 5a–c. Compared to other groups, the NaSH@CeO_2/CS-HA group consistently demonstrated accelerated healing of MRSA-infected wounds at all time points (p <0.05). Notably, wounds treated with

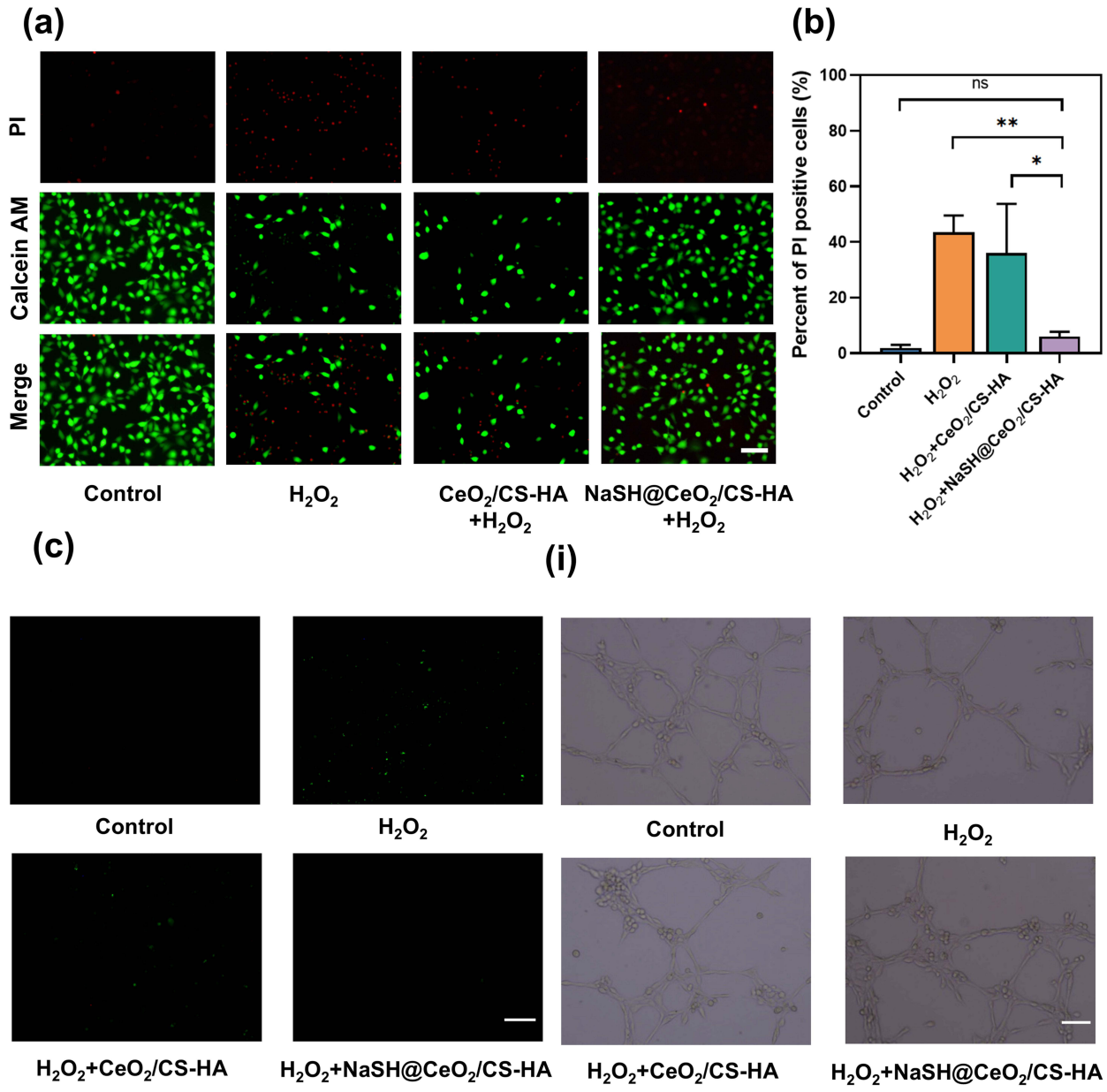

Figure 4 continued.

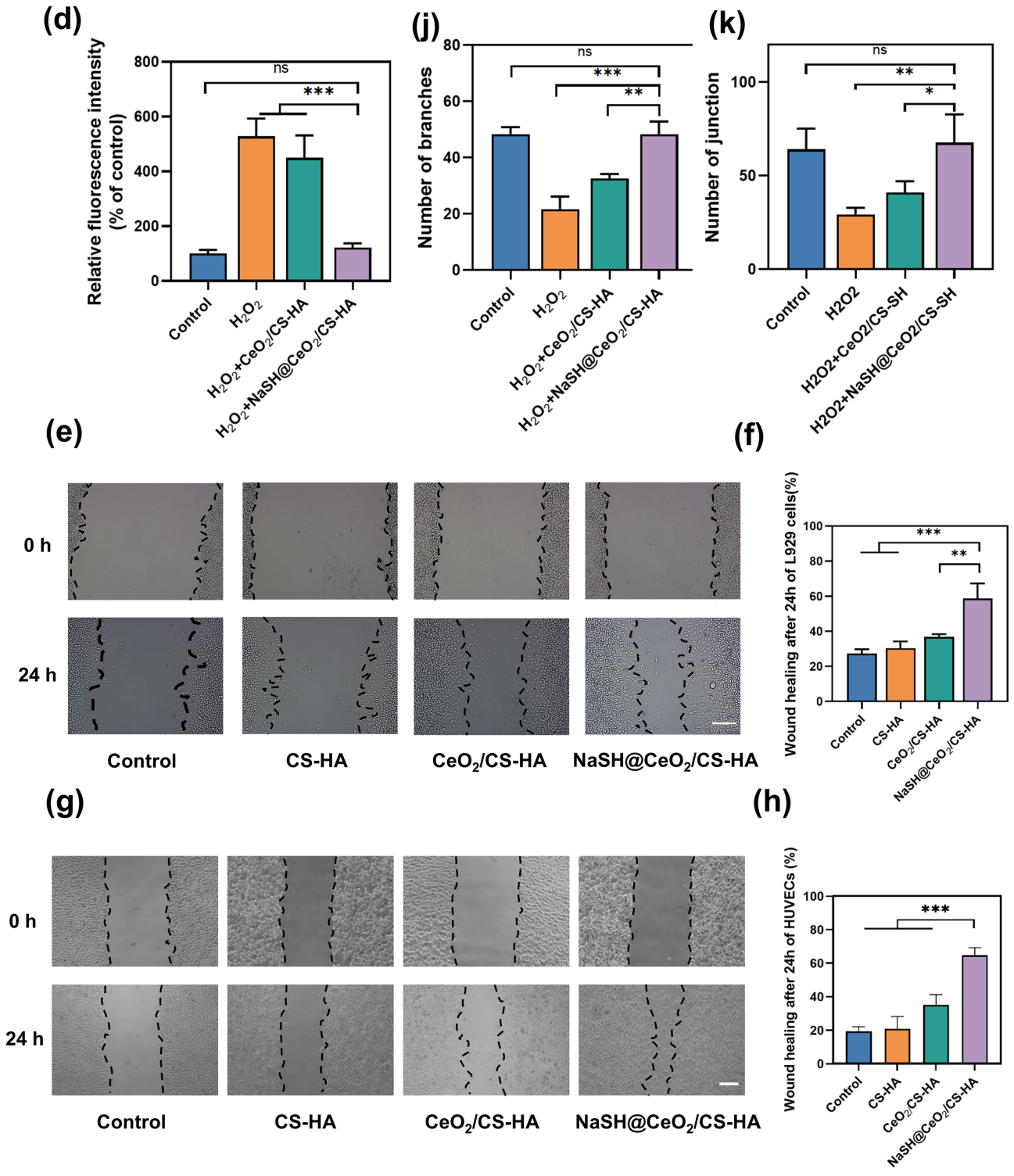

Figure 4 The effects of NaSH@CeO_2/CS-HA on wound healing induced. (**a**) Calcein-AM/PI assay was used to evaluate protect properties on OS induced by H_2O_2 in L929 cells and the results were quantitatively presented based on the (**b**) percent of PI position cells. The scale bar represents 100 μm. (**c** and **d**) DCFH-DA assay demonstrated the impact of NaSH@CeO_2/CS-HA on OS induced by H_2O_2, with the results illustrated using bar charts. The scale bar represents 100 μm. (**e** and **f**) Representative images and quantitative analysis of the scratch wound healing assay in L929 cells, treated with NaSH@CeO_2/CS-HA. The dashed lines in (**e**) indicate scratch edges. The healing rate is presented as the percentage of wound closure. The scale bar represents 200 μm. (**g** and **h**) Representative images and quantitative analysis of the scratch wound healing assay in HUVECs, treated with NaSH@CeO_2/CS-HA. The dashed lines in (**g**) indicate scratch edges. The healing rate is presented as the percentage of wound closure. The scale bar represents 100μm. (**i**) Tube formation assay was used to evaluate angiogenic properties, and the results were quantitatively presented based on the number of (**j**) junctions and (**k**) branches. The scale bar represents 100μm. The data represents the mean ±SD. (*$p < 0.05$, ** $p < 0.01$, *** $p < 0.001$, ns: no significant difference).

https://doi.org/10.2147/IJN.S538774

NaSH@CeO_2/CS-HA hydrogel were almost completely (98.13%) healed after 14 days, contrasting with the wounds in the other three groups (78.5%, 83.9%, and 88.9%).

To further assess skin wound healing, H&E and Masson three-color staining were used to evaluate the structure of the regenerated skin (Figure 5d and e). Based on scar length, H&E staining revealed considerable differences between NaSH@CeO_2/CS-HA and the other groups (Figure 5f). Additionally, Masson three-color staining showed that the wound area treated with NaSH@CeO_2/CS-HA had higher collagen density than the other three groups (Figure 5g, p <0.05). Collagen formation and deposition are key processes in wound healing, providing the structural framework for tissue regeneration.[64] These results further indicated that NaSH@CeO_2/CS-HA dressing could accelerate wound healing. Moreover, in the Masson tricolor staining results, a greater number of neovascularization were observed in the

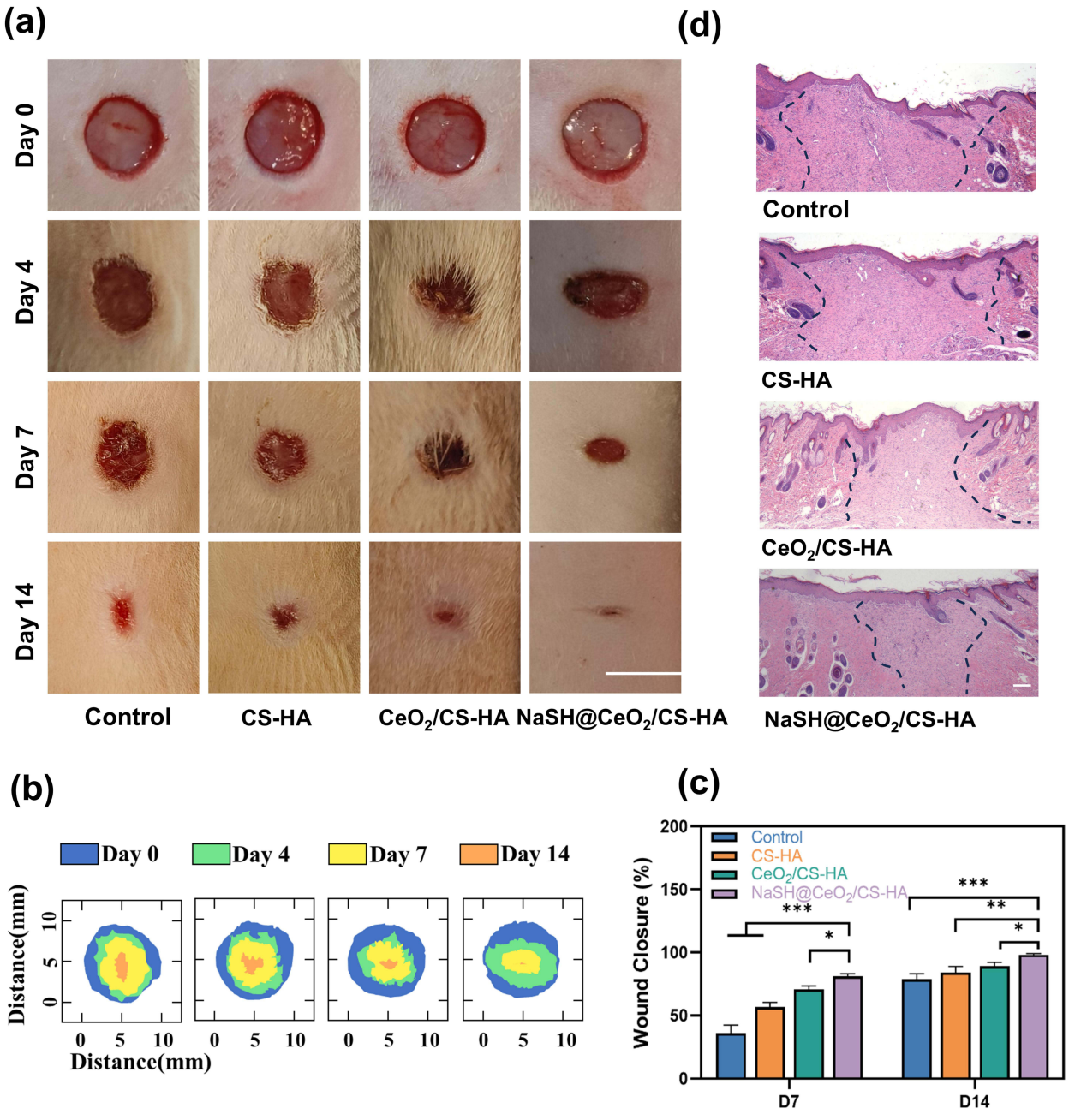

Figure 5 continued.

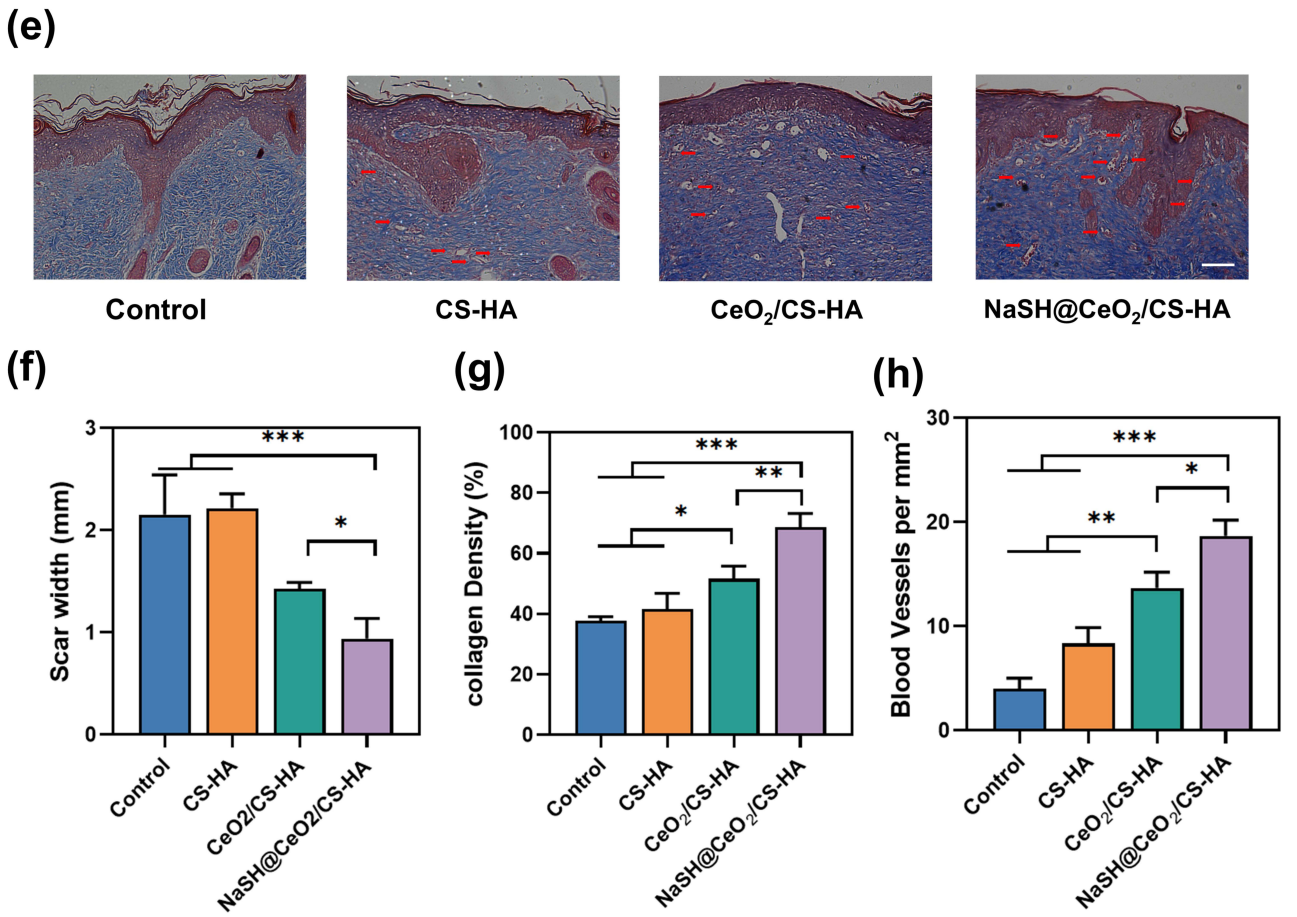

Figure 5 The wounds closure rate evaluation and histological analysis of infection wounds. (**a**) Representative images of diabetic wounds in different groups were captured on days 0, 4, 7, and 14 after surgery. The scale bar represents 1 cm. (**b**) A schematic diagram depicted the diabetic wounds healing process at different time points, and (**c**) the experimental results were graphically presented using a histogram on days 7 and 14. Histological analysis of infected wounds in each group was performed using (**d**) H&E staining and (**e**) Masson's trichrome staining at day 14; The dashed lines in (**d**) indicate the wound boundaries. The scale bar represents 200 μm in these panels. The red arrows in (**e**) indicate blood vessels. Quantitative analysis was conducted for (**f**) scar width, (**g**) collagen density, and (**h**) vascular density across all groups. The data represents the mean ±SD. (*$p < 0.05$, ** $p < 0.01$, *** $p < 0.001$).

regenerated skin tissue treated by the NaSH@CeO_2/CS-HA group, associated with an increase in the wound vascular system (Figure 5h).

Excessive OS plays a crucial role in the healing of chronic infected wounds. Bacterial infections lead to the accumulation of inflammatory cells, resulting in high levels of ROS that impair angiogenesis.[65] Additionally, excessive ROS disrupt cellular components such as DNA and lipids, triggering cell apoptosis and inhibiting wound healing.[66] To assess angiogenesis, we used immunofluorescence staining to detect the endothelial-specific marker CD31 (Figure 6a).[67] The results showed that the density of CD31-position cells in the NaSH@CeO_2/CS-HA group was significantly higher than in the other groups on day 7 (Figure 6b, $p < 0.05$), indicating that NaSH@CeO_2/CS-HA enhances vascular regeneration in infected wound healing patients. Caspase-3 plays a crucial role in the execution phase of cell apoptosis, and its activation is considered a hallmark of apoptosis.[68] We evaluated Caspase-3 to assess cell apoptosis levels in each group (Figure 6c). The results demonstrated that the density of Caspase-3-position cells in the NaSH@CeO_2/CS-HA group was significantly lower than in the other groups, highlighting the strong protective effect of NaSH@CeO_2/CS-HA on infective wound tissue (Figure 6d, $p < 0.05$).

https://doi.org/10.2147/IJN.S538774

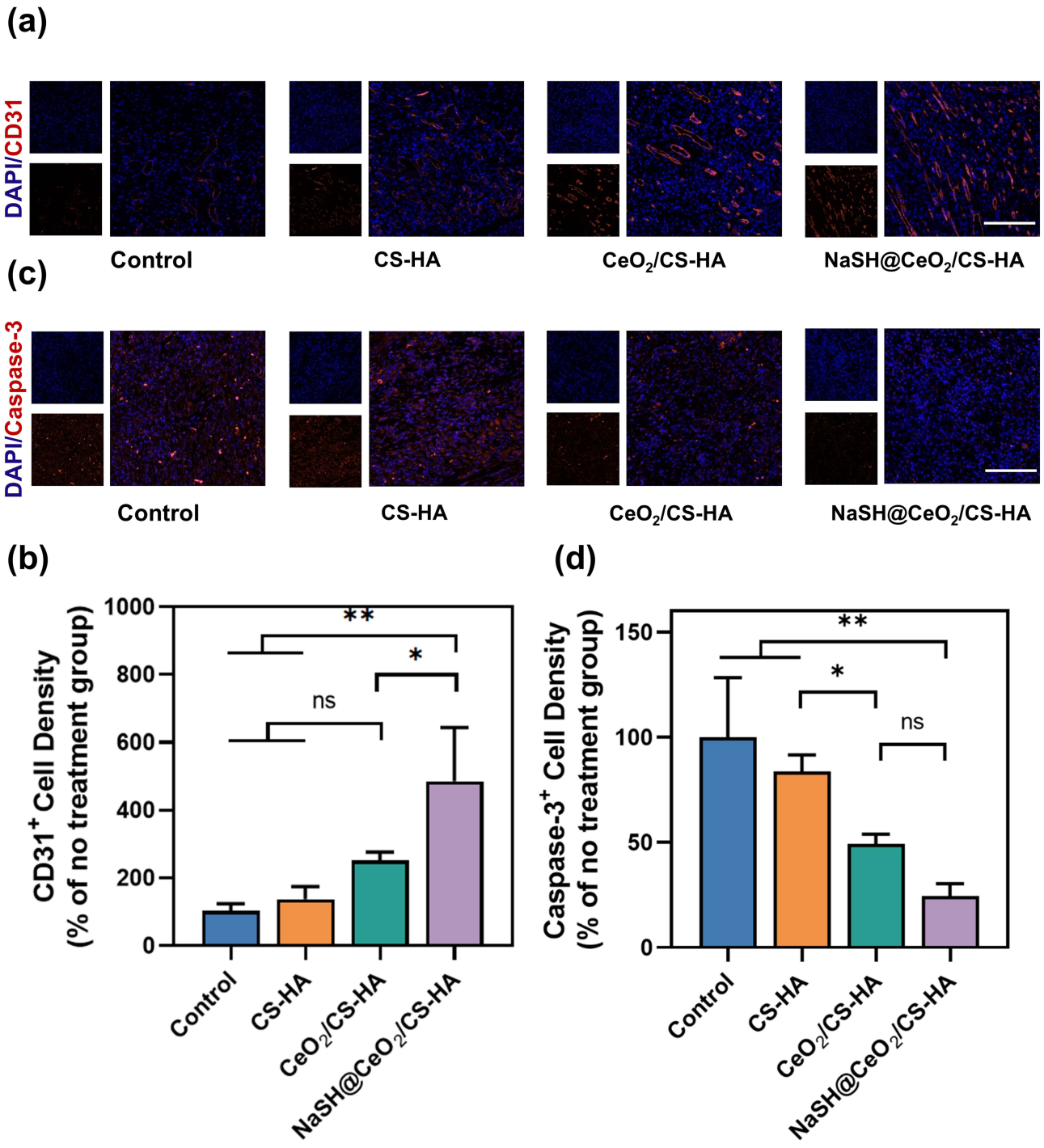

Figure 6 The immunofluorescence histological analysis of infection wounds. (**a** and **b**) Representative photographs and percent of position cell of CD31 immunofluorescence staining at the site of infection wounds 7 days after surgery were shown. The scale bar represents 200 μm. (**c** and **d**) The cleaved caspase-3 immunofluorescence staining was performed on day 7 after surgery, and cleaved caspase-3 expression was quantitatively assessed. The scale bar represents 200 μm. The data represents the mean ± SD. (*$p < 0.05$, ** $p < 0.01$, ns: no significant difference).

Discussion

In our study, we prepared a multi-functional bioactive material with slow-release gas molecules (NaSH@CeO_2/CS-HA). This formulation slowly releases H_2S into skin wounds to accelerate wound closure, while CeO_2-NPs control wound infection. Further investigations using cells and animal models demonstrated that NaSH@CeO_2/CS-HA has

a cytoprotective effect under the dual action of bacterial infection and OS, while also promoting cell migration and angiogenesis. From a clinical perspective, this material meets multi-functional requirements.

The CS-HA hydrogel was prepared by physical crosslinking method. The hydrogel design leverages the ionization properties of CS in an acidic environment, where its amino groups carry positive charges. HA, with carboxyl groups on its surface, interacts electrostatically with the ionized CS to form a physically crosslinked hydrogel. As depicted in Figure 1c, the three-dimensional network structure of CS-HA hydrogel is relatively uniform, with large pores, thin pore walls, and brittle structure, likely contributing to its high swelling capacity and low hardness. As shown in Figure 1h, hydrogels exhibit better adhesion to tissues and various substrates, possibly due to their hydrogen-rich composition, which enables noncovalent interactions.[69,70] At the same time, the low modulus of hydrogels provides mechanical strength suitable for skin adhesion.[71] In addition, nitrogen adsorption-desorption tests of CeO_2 demonstrate that the hollow CeO_2-NPs we successfully synthesized possess uniform mesoporous channels and extremely high specific surface areas, providing abundant loading sites and enormous loading capacities as drug carriers, making them ideal for constructing highly efficient and controllable drug delivery systems. Figure 1e–g demonstrates that the slow release of H_2S gas was achieved by incorporating NaSH into hollow CeO_2-NPs and CS-HA. The high efficiency of the drug loading and delivery system of NaSH has been fully demonstrated through mesoporous structure parameters and H_2S generation data. Notably, it is worth noting that H_2S release is more significant under neutral and acidic conditions, which is consistent with the acidic environment typically found in chronic infected wounds. This sustained-release system is capable of maintaining therapeutic concentrations of H_2S and CeO_2-NPs.[72,73] This suggests that hollow mesoporous CeO_2-NPs enable sustained release and microenvironment-responsive release of H_2S, and also enable intelligent control of H_2S release kinetics through interactions between the carrier and the drug.

Figure 2 illustrates that the hydrogel dressing exhibits cell and tissue compatibility without compromising cell survival rate. Histological analysis of liver and kidney tissues showed no difference compared to the control group. S. aureus is a common cause of skin infections.[74] Figure 3 demonstrates the anti-MRSA activity of NaSH@CeO_2/CS-HA. Although the samples were evaluated using a relatively high bacterial density (approximately 10^6 CFU/mL), NaSH@CeO_2/CS-HA hydrogels may be even more effective in clinical practice, where actual bacterial loads encountered are often lower. Furthermore, NaSH@CeO_2/CS-HA also exhibited inhibition against the gram-negative bacteria E. coli. The broad-spectrum antibacterial effect, coupled with sustained release of loaded CeO_2-NPs, helps maintain effective drug concentrations after wound formation, reducing the risk of contamination. Interestingly, Figure 3 suggests that the presence of H_2S may enhance the antibacterial gram-negative effect of CeO_2-NPs against gram-negative bacteria. This enhancement could be attributed to the reduction of Ce^{4+} to Ce^{3+} upon contact with the bacterial surface, activating oxidative stress within the gram-negative bacteria,[75] and H_2S potentially promoting this reaction.[75]

ROS levels in local areas can lead to OS in surrounding tissues, damaging key biomolecules such as DNA, RNA, and enzymes, which ultimately hinders wound healing.[76] In Figure 4, we observe that hydrogel dressings reduce cell apoptosis under OS conditions. Further, DCFH-DA staining suggests that this decrease in apoptosis may be attributed to the reduction of excessive ROS levels in cells by NaSH@CeO_2/CS-HA. Additionally, scratch test results indicate that the addition of H_2S enhanced the ability of CeO_2-NPs to promote cell migration. Simultaneously, H_2S enhances tube formation under OS, highlighting its protective effect and potential to promote angiogenesis.

Untreated wound infections lead to the accumulation of persistent inflammatory cells, resulting in excessive ROS secretion within the wound site. This excessive superoxide production damages surrounding tissues and disrupts the normal wound regeneration process.[77,78] Our MRSA-infected, difficult-to-heal full-thickness skin defect model and in vivo experimental results further confirm that NaSH@CeO_2/CS-HA not only accelerates wound healing but also promotes skin repair in cases of severe infection. While CeO_2-NPs ablates invading bacteria and reduces external pathogen interference, H_2S mitigates ROS levels, creating a pro-regenerative microenvironment that supports skin regeneration and collagen formation. The functional status of local blood vessels is critical for treating infected wounds. High ROS concentration impairs angiogenic ability and compromises vascular integrity, hindering wound healing.[67,79] Therefore, immunofluorescence staining results demonstrate that the addition of H_2S enhances cell protection and angiogenesis function under OS. Overall, NaSH@CeO_2/CS-HA hydrogel holds promise for clinical applications due

 https://doi.org/10.2147/IJN.S538774

to its multifunctional advantages, including infection prevention, rapid wound healing promotion, and angiogenesis support.

Although NaSH@CeO_2/CS-HA hydrogel has shown good efficacy in infectious non-healing wounds, its role in long-term chronic wounds requires further study. Additionally, although in vitro and in vivo experiments have comprehensively demonstrated that the material releases H_2S and exerts its function in the microenvironment of infected wounds, the lack of real-time, dynamic in vivo H_2S kinetic data is also one of the limitations of this study.

Conclusion

In this study, we successfully synthesized a novel hydrogel dressing with integrated antioxidant, antibacterial, and wound-healing-promoting properties, which is suitable for the clinical treatment of refractory infected wounds. The hydrogel is primarily composed of chitosan and hyaluronic acid, and is loaded with a NaSH@CeO_2 complex to enable the controlled release of CeO_2-NPs and H_2S. In the infected wound microenvironment, the NaSH@CeO_2/CS–HA hydrogel responsively releases CeO_2-NPs, which exhibit significant antibacterial activity and effectively inhibit bacterial growth. Furthermore, the controllably released H_2S promotes cell proliferation and migration. Notably, NaSH@CeO_2 /CS–HA also counteracts OS-induced apoptosis and enhances angiogenesis, thereby accelerating the healing of infected wounds. Overall, NaSH@CeO_2/CS–HA demonstrates excellent biocompatibility and holds great potential for clinical application in the management of refractory infected wounds. However, further regulatory oversight is still required to address issues related to raw material control, stability, and the therapeutic window.

Data Sharing Statement

The data are available within the paper or are available from Qiugen Wang upon request.

Ethical Approval and Consent to Participate

The animal study was examined and approved by the Institutional Review Board of Shanghai First People's Hospital (IACUC number: 2024AWS468).

Consent for Publication

All authors agree to submit for publication in "International Journal of Nanomedicine".

Acknowledgments

This work was supported by National Natural Science Foundation of China (No. 82172443).

Disclosure

The authors declare no competing interests.

References

1. Ramirez GA, Viel TA. Potential of natural senolytic compounds in eliminating senescent cells and alleviating age-related skin deterioration: a narrative review. *Aging Advances*. 2024;1(2):143–153. doi:10.4103/AGINGADV.AGINGADV-D-24-00014
2. Jones RE, Foster DS, Longaker MT. Management of Chronic Wounds-2018. *JAMA*. 2018;320(14):1481–1482. doi:10.1001/jama.2018.12426
3. Zhang J, Yang P, Liu D, et al. Inhibiting Hyper-O-GlcNAcylation of c-Myc accelerate diabetic wound healing by alleviating keratinocyte dysfunction. *Burns Trauma*. 2021;9:tkab031.
4. Bahadoran Z, Mirmiran P, Hosseinpanah F, Kashfi K, Ghasemi A. Nitric oxide-based treatments improve wound healing associated with diabetes mellitus. *Med Gas Res*. 2025;15(1):23–35. doi:10.4103/mgr.MEDGASRES-D-24-00020
5. Wang L, Ding X, Fan L, et al. Self-healing dynamic hydrogel microparticles with structural color for wound management. *Nanomicro Lett*. 2024;16 (1):232. doi:10.1007/s40820-024-01422-4
6. Fallah N, Rasouli M, Amini MR. The current and advanced therapeutic modalities for wound healing management. *J Diabetes Metab Disord*. 2021;20(2):1883–1899. doi:10.1007/s40200-021-00868-2
7. Hu P, Yang Q, Wang Q, et al. Mesenchymal stromal cells-exosomes: a promising cell-free therapeutic tool for wound healing and cutaneous regeneration. *Burns Trauma*. 2019;7:38. doi:10.1186/s41038-019-0178-8
8. Jiang T, Li Q, Qiu J, et al. Nanobiotechnology: applications in chronic wound healing. *Int J Nanomed*. 2022;17:3125–3145. doi:10.2147/IJN.S372211

9. Las Heras K, Garcia-Orue I, Rancan F, Igartua M, Santos-Vizcaino E, Hernandez RM. Modulating the immune system towards a functional chronic wound healing: a biomaterials and nanomedicine perspective. *Adv Drug Deliv Rev*. 2024;210:115342. doi:10.1016/j.addr.2024.115342
10. Gong YR, Zhang C, Xiang X, et al. Baicalin, silver titanate, Bletilla striata polysaccharide and carboxymethyl chitosan in a porous sponge dressing for burn wound healing. *J Integr Med*. 2023;21(5):487–495. doi:10.1016/j.joim.2023.07.002
11. Chen Y, Xu Y, Ramakrishna S. Electromagnetic-responsive targeted delivery scaffold technology has better potential to repair injured peripheral nerves: a narrative review. *Adv Technol Neurosci*. 2024;1(1):51–71.
12. André-Lévigne D, Modarressi A, Pepper MS, Pittet-Cuénod B. Reactive oxygen species and NOX enzymes are emerging as key players in cutaneous wound repair. *Int J Mol Sci*. 2017;18(10):2149. doi:10.3390/ijms18102149
13. Jeon HH, Yu Q, Lu Y, et al. FOXO1 regulates VEGFA expression and promotes angiogenesis in healing wounds. *J Pathol*. 2018;245(3):258–264. doi:10.1002/path.5075
14. Jekhmane S, Derks MGN, Maity S, et al. Host defence peptide plectasin targets bacterial cell wall precursor lipid II by a calcium-sensitive supramolecular mechanism. *Nat Microbiol*. 2024;9(7):1778–1791. doi:10.1038/s41564-024-01696-9
15. Ma C, Tian X, Kim JP, et al. Citrate-based materials fuel human stem cells by metabonegenic regulation. *Proc Natl Acad Sci U S A*. 2018;115(50):E11741–e50. doi:10.1073/pnas.1813000115
16. Cheng H, Shi Z, Yue K, et al. Sprayable hydrogel dressing accelerates wound healing with combined reactive oxygen species-scavenging and antibacterial abilities. *Acta Biomater*. 2021;124:219–232. doi:10.1016/j.actbio.2021.02.002
17. Li C, Chen J, Deng G, et al. A pH-Sensitive and mitochondria-modulating intelligent multilayered dressing system for a comprehensive therapeutic strategy of diabetic wounds. *Composites Part B*. 2023;266:110984. doi:10.1016/j.compositesb.2023.110984
18. Lan J, Shi L, Xiao W, Zhang X, Wang S. A rapid self-pumping organohydrogel dressing with hydrophilic fractal microchannels to promote burn wound healing. *Adv Mater*. 2023;35(38):e2301765. doi:10.1002/adma.202301765
19. Han X, Wang L, Shang Y, Liu X, Yuan J, Shen J. Hydrogen sulfide-releasing polyurethane/gelatin/keratin-TA conjugate mats for wound healing. *J Mater Chem B*. 2022;10(42):8672–8683. doi:10.1039/D2TB01700H
20. Magli E, Perissutti E, Santagada V, et al. H(2)S donors and their use in medicinal chemistry. *Biomolecules*. 2021;11(12):1899. doi:10.3390/biom11121899
21. Zimmermann KK, Spassov SG, Strosing KM, et al. Hydrogen sulfide exerts anti-oxidative and anti-inflammatory effects in acute lung injury. *Inflammation*. 2018;41(1):249–259. doi:10.1007/s10753-017-0684-4
22. Wang C, Deng Y, Liu Z, Liao W. Hydrogen sulfide in plants: crosstalk with other signal molecules in response to abiotic stresses. *Int J Mol Sci*. 2021;22(21):12068. doi:10.3390/ijms222112068
23. Yang CT, Chen L, Chen WL, et al. Hydrogen sulfide primes diabetic wound to close through inhibition of NETosis. *Mol Cell Endocrinol*. 2019;480:74–82. doi:10.1016/j.mce.2018.10.013
24. Abdel Latef AAH, Dawood MFA, Hassanpour H, Rezayian M, Younes NA. Impact of the static magnetic field on growth, pigments, osmolytes, nitric oxide, hydrogen sulfide, phenylalanine ammonia-lyase activity, antioxidant defense system, and yield in lettuce. *Biology*. 2020;9(7):172. doi:10.3390/biology9070172
25. Papapetropoulos A, Pyriochou A, Altaany Z, et al. Hydrogen sulfide is an endogenous stimulator of angiogenesis. *Proc Natl Acad Sci U S A*. 2009;106(51):21972–21977. doi:10.1073/pnas.0908047106
26. Coavoy-Sánchez SA, Costa SKP, Muscará MN. Hydrogen sulfide and dermatological diseases. *Br J Pharmacol*. 2020;177(4):857–865. doi:10.1111/bph.14699
27. Shi X, Li H, Guo F, Li D, Xu F. Novel ray of hope for diabetic wound healing: hydrogen sulfide and its releasing agents. *J Adv Res*. 2024;58:105–115. doi:10.1016/j.jare.2023.05.009
28. Glanville JRW, Jalali P, Flint JD, et al. Potent anti-inflammatory effects of an H(2) S-releasing naproxen (ATB-346) in a human model of inflammation. *FASEB j*. 2021;35(10):e21913. doi:10.1096/fj.201902918RR
29. Wen X, Ye Y, Yu Z, Shen H, Cui G, Chen G. The role of nitric oxide and hydrogen sulfide in spinal cord injury: an updated review. *Med Gas Res*. 2024;14(3):96–101. doi:10.4103/2045-9912.385946
30. Zhao H, Lu S, Chai J, et al. Hydrogen sulfide improves diabetic wound healing in ob/ob mice via attenuating inflammation. *J Diabetes Complications*. 2017;31(9):1363–1369. doi:10.1016/j.jdiacomp.2017.06.011
31. Hu Q, Wu D, Ma F, et al. Novel angiogenic activity and molecular mechanisms of ZYZ-803, a slow-releasing hydrogen sulfide-nitric oxide hybrid molecule. *Antioxid Redox Signal*. 2016;25(8):498–514. doi:10.1089/ars.2015.6607
32. Khurshid F, Iqbal J, Ahmad FU, et al. A combination of generated hydrogen sulfide and nitric oxide activity has a potentiated protectant effect against cisplatin induced nephrotoxicity. *Heliyon*. 2024;10(8):e29513. doi:10.1016/j.heliyon.2024.e29513
33. Andrés CMC, Pérez de la Lastra JM, Andrés Juan C, Plou FJ, Pérez-Lebeña E. Chemistry of hydrogen sulfide-pathological and physiological functions in mammalian cells. *Cells*. 2023;12(23):2684. doi:10.3390/cells12232684
34. Lin WC, Huang CC, Lin SJ, et al. In situ depot comprising phase-change materials that can sustainably release a gasotransmitter H(2)S to treat diabetic wounds. *Biomaterials*. 2017;145:1–8. doi:10.1016/j.biomaterials.2017.08.023
35. Chen M, Xu T, Song L, et al. Nanotechnology based gas delivery system: a "green" strategy for cancer diagnosis and treatment. *Theranostics*. 2024;14(14):5461–5491. doi:10.7150/thno.98884
36. Ghaffari-Bohlouli P, Jafari H, Okoro OV, et al. Gas therapy: generating, delivery, and biomedical applications. *Small Methods*. 2024;8(8):e2301349. doi:10.1002/smtd.202301349
37. Charbgoo F, Ahmad MB, Darroudi M. Cerium oxide nanoparticles: green synthesis and biological applications. *Int J Nanomed*. 2017;12:1401–1413. doi:10.2147/IJN.S124855
38. Sedighi M, Rahimi F, Shahbazi MA, et al. Controlled tyrosine kinase inhibitor delivery to liver cancer cells by gate-capped mesoporous silica nanoparticles. *ACS Appl Bio Mater*. 2020;3(1):239–251. doi:10.1021/acsabm.9b00772
39. Molavi H. Cerium-based metal-organic frameworks: synthesis, properties, and applications. *Coord Chem Rev*. 2025;527:216405.
40. Silina EV, Manturova NE, Ivanova OS, et al. Cerium dioxide-dextran nanocomposites in the development of a medical product for wound healing: physical. *Chem Biomed Characteristics Mol*. 2024;29(12):2853.
41. Xue Y, Yang F, Wu L, Xia D, Liu Y. CeO(2) nanoparticles to promote wound healing: a systematic review. *Adv Healthc Mater*. 2024;13(6):e2302858. doi:10.1002/adhm.202302858

42. Francoleon NE, Carrington SJ, Fukuto JM. The reaction of H(2)S with oxidized thiols: generation of persulfides and implications to H(2)S biology. *Arch Biochem Biophys*. 2011;516(2):146–153. doi:10.1016/j.abb.2011.09.015
43. Huang Y, Ren J, Qu X. Nanozymes: classification, catalytic mechanisms, activity regulation, and applications. *Chem Rev*. 2019;119(6):4357–4412. doi:10.1021/acs.chemrev.8b00672
44. Lu H, Wan L, Li X, et al. Combined synthesis of cerium oxide particles for effective anti-bacterial and anti-cancer nanotherapeutics. *Int J Nanomed*. 2022;17:5733–5746. doi:10.2147/IJN.S379689
45. Krishna Moorthy SB, Mariappan A, Tsai TY, Kao TH, Inbaraj B, Chen B-H. Cytotoxicity and antibacterial activity of gold-supported cerium oxide nanoparticles. *Int J Nanomed*. 2014;9:5515–5531. doi:10.2147/IJN.S70087
46. Zhang Y, Liu S, Peng J, et al. Biomimetic nanozymes suppressed ferroptosis to ameliorate doxorubicin-induced cardiotoxicity via synergetic effect of antioxidant stress and GPX4 restoration. *Nutrients*. 2023;15(5):1090.
47. Osi AR, Zhang H, Chen J, et al. Three-dimensional-printable thermo/photo-cross-linked methacrylated chitosan-gelatin hydrogel composites for tissue engineering. *ACS Appl Mater Interfaces*. 2021;13(19):22902–22913. doi:10.1021/acsami.1c01321
48. Fang W, Yang L, Hong L, Hu Q. A chitosan hydrogel sealant with self-contractile characteristic: from rapid and long-term hemorrhage control to wound closure and repair. *Carbohydr Polym*. 2021;271:118428. doi:10.1016/j.carbpol.2021.118428
49. Roas-Escalona N, Becquart F, Delair T, Dutertre F. Chitosan-based hydrogels: influence of crosslinking strategy on rheological properties. *Carbohydr Polym*. 2024;341:122329. doi:10.1016/j.carbpol.2024.122329
50. Ji S, Zhao Y, Zhai X, et al. A dual-crosslinked hydrogel based on gelatin methacryloyl and sulfhydrylated chitosan for promoting wound healing. *Int J Mol Sci*. 2023;24(3):2447. doi:10.3390/ijms24032447
51. Griffin DR, Archang MM, Kuan CH, et al. Activating an adaptive immune response from a hydrogel scaffold imparts regenerative wound healing. *Nat Mater*. 2021;20(4):560–569. doi:10.1038/s41563-020-00844-w
52. Chen Y, Liu X, Liu R, et al. Zero-order controlled release of BMP2-derived peptide P24 from the chitosan scaffold by chemical grafting modification technique for promotion of osteogenesis in vitro and enhancement of bone repair in vivo. *Theranostics*. 2017;7(5):1072–1087. doi:10.7150/thno.18193
53. Lee SJ, Seok JM, Lee JH, Lee J, Kim WD, Park SA. Three-dimensional printable hydrogel using a hyaluronic acid/sodium alginate bio-ink. *Polymers*. 2021;13(5):794.
54. Zhang R, Li H, Zhang W, et al. Chlorogenic acid/carboxymethyl chitosan nanoparticle-assisted biomultifunctional hyaluronic acid-based hydrogel scaffolds for burn skin repair. *Int J Biol Macromol*. 2024;275(Pt 1):133528. doi:10.1016/j.ijbiomac.2024.133528
55. Li J, Chen C, Xia T. Understanding nanomaterial-liver interactions to facilitate the development of safer nanoapplications. *Adv Mater*. 2022;34(11):e2106456. doi:10.1002/adma.202106456
56. Tsoi KM, MacParland SA, Ma XZ, et al. Mechanism of hard-nanomaterial clearance by the liver. *Nat Mater*. 2016;15(11):1212–1221. doi:10.1038/nmat4718
57. Sarkar K, Dutta K, Chatterjee A, et al. Nanotherapeutic potential of antibacterial folic acid-functionalized nanoceria for wound-healing applications. *Nanomedicine*. 2023;18(2):109–123. doi:10.2217/nnm-2022-0233
58. Wu J, Wu Y, Tang H, et al. Self-adapting biomass hydrogel embodied with miRNA immunoregulation and long-term bacterial eradiation for synergistic chronic wound therapy. *ACS Nano*. 2024;18:18379–92.
59. Hou B, Li B, Deng W, et al. DHTPY-Cu@ZOL-enhanced photodynamic therapy: a strategic platform for advanced treatment of drug-resistant bacterial wound infections. *Int J Nanomed*. 2024;19:6319–6336. doi:10.2147/IJN.S458520
60. Guo J, Zhang X, Mao R, et al. Multifunctional glycopeptide-based hydrogel via dual-modulation for the prevention and repair of radiation-induced skin injury. *ACS Biomater Sci Eng*. 2024;10(8):5168–5180. doi:10.1021/acsbiomaterials.4c00698
61. Sies H. Hydrogen peroxide as a central redox signaling molecule in physiological oxidative stress: oxidative eustress. *Redox Biol*. 2017;11:613–619. doi:10.1016/j.redox.2016.12.035
62. Andrabi SM, Majumder S, Gupta KC, Kumar A. Dextran based amphiphilic nano-hybrid hydrogel system incorporated with curcumin and cerium oxide nanoparticles for wound healing. *Colloids Surf B Biointerfaces*. 2020;195:111263. doi:10.1016/j.colsurfb.2020.111263
63. Liu W, Gao R, Yang C, et al. ECM-mimetic immunomodulatory hydrogel for methicillin-resistant Staphylococcus aureus-infected chronic skin wound healing. *Sci Adv*. 2022;8(27):eabn7006. doi:10.1126/sciadv.abn7006
64. Li W, Bei Y, Pan X, et al. Selenide-linked polydopamine-reinforced hybrid hydrogels with on-demand degradation and light-triggered nanozyme release for diabetic wound healing. *Biomater Res*. 2023;27(1):49. doi:10.1186/s40824-023-00367-w
65. Guan Y, Niu H, Liu Z, et al. Sustained oxygenation accelerates diabetic wound healing by promoting epithelialization and angiogenesis and decreasing inflammation. *Sci Adv*. 2021;7(35). doi:10.1126/sciadv.abj0153
66. Augustine R, Zahid AA, Hasan A, Dalvi YB, Jacob J. Cerium oxide nanoparticle-loaded gelatin methacryloyl hydrogel wound-healing patch with free radical scavenging activity. *ACS Biomater Sci Eng*. 2021;7(1):279–290. doi:10.1021/acsbiomaterials.0c01138
67. Liu X, Han X, Shang Y, Wang L, Shen J, Yuan J. Hydrogen sulfide releasing poly(γ-glutamic acid) biocomposite hydrogel with monitoring, antioxidant, and antibacterial properties for diabetic wound healing. *Int J Biol Macromol*. 2023;253(Pt 6):127053. doi:10.1016/j.ijbiomac.2023.127053
68. Liu Q, Liu C, Lei B. siRNA mediated downregulation of RhoA expression reduces oxidative induced apoptosis in retinal ganglion cells. *Curr Mol Med*. 2024;24(5):630–636. doi:10.2174/1566524023666230511095628
69. Qian Y, Zheng Y, Jin J, et al. Immunoregulation in diabetic wound repair with a photoenhanced glycyrrhizic acid hydrogel scaffold. *Adv Mater*. 2022;34(29):e2200521. doi:10.1002/adma.202200521
70. An H, Gu Z, Zhou L, et al. Janus mucosal dressing with a tough and adhesive hydrogel based on synergistic effects of gelatin, polydopamine, and nano-clay. *Acta Biomater*. 2022;149:126–138. doi:10.1016/j.actbio.2022.07.016
71. Chen A, Wu L, Wang K, et al. Facile synthesis of rapid hemostatic powder based on sodium alginate for promoting hemostasis and wound healing. *Int J Biol Macromol*. 2025;308(Pt 4):142728. doi:10.1016/j.ijbiomac.2025.142728
72. Ma M, Zhong Y, Jiang X. Thermosensitive and pH-responsive tannin-containing hydroxypropyl chitin hydrogel with long-lasting antibacterial activity for wound healing. *Carbohydr Polym*. 2020;236:116096. doi:10.1016/j.carbpol.2020.116096
73. Gao Y, Ma Q. Bacterial infection microenvironment-responsive porous microspheres by microfluidics for promoting anti-infective therapy. *Smart Medicine*. 2022;1(1):e20220012. doi:10.1002/SMMD.20220012

74. Chessa D, Ganau G, Spiga L, et al. Staphylococcus aureus and staphylococcus epidermidis virulence strains as causative agents of persistent infections in breast implants. *PLoS One*. 2016;11(1):e0146668. doi:10.1371/journal.pone.0146668
75. Thill A, Zeyons O, Spalla O, et al. Cytotoxicity of CeO2 nanoparticles for Escherichia coli. Physico-chemical insight of the cytotoxicity mechanism. *Environ Sci Technol*. 2006;40(19):6151–6156. doi:10.1021/es060999b
76. Gao L, Feng Q, Cui B, et al. Loading Nanoceria Improves Extracellular Vesicle Membrane Integrity and Therapy to Wounds in Aged Mice. *ACS Biomater Sci Eng*. 2023;9(2):732–742. doi:10.1021/acsbiomaterials.2c01104
77. He J, Meng X, Meng C, et al. Layer-by-layer pirfenidone/cerium oxide nanocapsule dressing promotes wound repair and prevents scar formation. *Molecules*. 2022;27(6):1830.
78. Hao J, Liu C, Zhou L, et al. Enhancing diabetic wound healing with a pH/glucose dual-responsive hydrogel for ROS clearance and antibacterial activity. *Int J Biol Macromol*. 2024;272(Pt 2):132935. doi:10.1016/j.ijbiomac.2024.132935
79. Wu Y, Wu Q, Fan X, et al. Study on chitosan/gelatin hydrogels containing ceria nanoparticles for promoting the healing of diabetic wound. *J Biomed Mater Res A*. 2024;112(9):1532–1547. doi:10.1002/jbm.a.37701